

0084

REPORT DOCUMENTATION PAGE		
<p>Public reporting burden for this collection of information is estimated to average 1 hour per response, including the time for reviewing instructions, completing and reviewing this collection of information. Send comments regarding this burden estimate or any other reducing this burden to Washington Headquarters Services, Directorate for Information Operations and Reports, 1215 Jefferson Davis Highway, Suite 1204, Arlington, VA 22202-4302, Attention: Director, Report Burden Reduction Project (0704-0188), Washington, DC 20503.</p>		
1. AGENCY USE ONLY (Leave blank)	2. REPORT DATE 12/18/03	3. REPORT TYPE AND DATES COVERED AMENDMENT 09/01/02 - 12/31/03 Final
4. TITLE AND SUBTITLE INTRINSIC LEFT-HANDED METAMATERIALS RESEARCH		5. FUNDING NUMBERS AFOSR F49620-02-1-0404
6. AUTHOR(S) SCHULTZ, SHELDON		
7. PERFORMING ORGANIZATION NAME(S) AND ADDRESS(ES) UNIVERSITY OF CALIFORNIA SAN DIEGO - THE REGENTS OFFICE OF CONTRACTS AND GRANTS 9905 GILMAN DRIVE LA JOLLA, CA 92093-0319		8. PERFORMING ORGANIZATION REPORT NUMBER 27322A
9. SPONSORING / MONITORING AGENCY NAME(S) AND ADDRESS(ES) DR. HAROLD WEINSTOCK, AFOSR/NE (703) 696-8572 USAF, AFRL AF OFFICE OF SCIENTIFIC RESEARCH 801 N. RANDOLPH ST., ROOM 732 ARLINGTON, VA 22203-1977		10. SPONSORING / MONITORING AGENCY REPORT NUMBER AFOSR/PKC 1
11. SUPPLEMENTARY NOTES 20040213 107		
12a. DISTRIBUTION / AVAILABILITY STATEMENT DISTRIBUTE FREELY Distribution Statement A: APPROVED FOR PUBLIC RELEASE BY RELEASER UNLIMITED		
13. ABSTRACT (Maximum 200 Words)		
<p>In this Final Report we present results for both areas of research and potential applications for the novel Left-Handed MetaMaterials (LHM) which our group has previously discovered. In Section I, we report advances made in our laboratory in instrumentation and simulations that focussed on the utilization of LHM that can serve as backplanes for antennas with improved radiative properties. In Section II we discuss preliminary measurements on the incorporation of regions of paramagnetic spins into the LHM structure so as to permit magnetic field modulation of the Split Ring Resonators which provide the negative permeability of the sample. In Section III we report on our efforts to create a cooperative program with a suggested industrial manufacturer for utilization of high Tc superconducting components in LHM of interest.</p>		
14. SUBJECT TERMS LEFT-HANDED METAMATERIALS PERMITTIVITY AND PERMEABILITY		15. NUMBER OF PAGES 11 PAGES 16. PRICE CODE
17. SECURITY CLASSIFICATION OF REPORT SAR	18. SECURITY CLASSIFICATION OF THIS PAGE UU	19. SECURITY CLASSIFICATION OF ABSTRACT UU
20. LIMITATION OF ABSTRACT		

NSN 7540-01-280-5500

Standard Form 298 (Rev. 2-89)
Prescribed by ANSI Std. Z39-18
298-102

Intrinsic Left-Handed Metamaterials Research

Sheldon Schultz and David R. Smith

Abstract

In this Final Report we present results for both areas of research and potential applications for the novel Left-Handed MetaMaterials (LHM) which our group has previously discovered. In Section I, we report advances made in our laboratory in instrumentation and simulations that focussed on the utilization of LHM that can serve as backplanes for antennas with improved radiative properties. In Section II we discuss preliminary measurements on the incorporation of regions of paramagnetic spins into the LHM structure so as to permit magnetic field modulation of the Split Ring Resonators which provide the negative permeativity of the sample. In Section III we report on our efforts to create a cooperative program with a suggested industrial manufacturer for utilization of high Tc superconducting components in LHM of interest.

I. Metamaterials as Antenna Substrates

Our goal in this part of our program was to evaluate metamaterials for application as novel antenna substrates or radomes for communications applications. Ultimately, our goal is to incorporating active elements into a metamaterial, thereby implementing dynamic beam steering or other mechanisms of novel RF control. Before this ultimate goal can be realized, however, there are several crucial steps that need to be completed as part of this overall program; in particular,

1. The ability to rapidly simulate and fabricate prototype metamaterial samples must be in place.
2. We need to have an efficient fabrication and reliable test apparatus to enable quick confirmation of the expected material properties.
3. For passive materials, we need to evaluate metamaterial structures that indicate particular advantages and capabilities either not present in existing materials or exhibit substantial improvements.
4. For dynamic tuning, we need to evaluate two or more material properties—or “states” of material, which will significantly modify the radiation pattern associated with a nearby antenna, and the means to switch between these states.
5. For the most flexible control uses, we need to perform a systematic analysis of the possibilities inherent to a reconfigurable material whose material properties can be adjusted spatially, on a scale less than the wavelength (i.e., at the unit cell level).

In this phase of the project, we have developed the groundwork that will enable the future goals of the project to be realized. Specifically, in this project period we have:

1. Improved our metamaterial development cycle time. Under separate funding, we have obtained an LPKF ProtoMat circuit board prototype numerically controlled milling machine, capable of producing appropriate sized metamaterial samples within one or two days.
2. Modified our Angle-Resolved Microwave Spectrometer (ARMS) to allow antenna gain measurements from a coaxial fed antenna. We have systematically improved the reproducibility of the gain measurements to a level of less than 1% from scan to scan; with

DISTRIBUTION STATEMENT A

Approved for Public Release
Distribution Unlimited

- this sensitivity we can easily evaluate the antenna enhancements and even slight changes in gain.
3. Performed calibration measurements on low-impedance reflector planes to compare with expected gain curves.
 4. Measured metamaterial reflector planes and compared with expected gain curves based on the calculated material properties.

The measurements are preliminary and primarily made to test the feasibility of our methodology. In this section of the report, we describe the modifications to the ARMS apparatus, its sensitivity and limitations and the preliminary metamaterial measurements.

Modifications to the ARMS Apparatus

The ARMS apparatus was originally developed to better quantify the refraction properties of left-handed metamaterials. However, the apparatus is capable of probing a number of different metamaterial aspects, including the function of a metamaterial used as an antenna back plane.

The ARMS design follows in spirit that utilized originally to confirm the negative refractive index of a wedge-shaped metamaterial sample. The ARMS apparatus is based on the planar waveguide geometry shown in Fig. 1. Two parallel plates spaced nominally one centimeter apart are used to confine radiation to the plane. By restricting radiation in this manner, we minimize the necessary sample volume required for the measurements. The lowest mode of the planar waveguide has no cutoff and is characterized by an electric field polarized uniformly along the direction perpendicular to the plane of the waveguide plates. In the empty chamber, these modes have the identical dispersion characteristics of free space waves. Moreover, because the electric field is always polarized perpendicular to the plane of incidence, as defined by the propagation direction and the normal to any sample surface, the waveguide modes are equivalent to s-polarized waves. Note that while the confined geometry allows minimum sample sizes to be considered, the restriction to one polarization—s-polarization—is a distinct limitation that prevents a full sample characterization. However, the efficiency associated with smaller sample sizes and rapid sample characterization offset this disadvantage.

Of particular concern for this work is the possibility of reflection of the generated and scattered waves back into the scattering region, which could produce unwanted artifacts in the data. At all interfaces between the scattering chamber and free space, for example, there exists a substantial impedance mismatch that will reflect some portion of the radiation. A possible means of minimizing or eliminating this reflection would be to line the entire periphery of the chamber with microwave absorber; but this would reduce the signal reaching the external detector, complicate the design and possibly also produce artifacts in the data. A compromise absorber pattern is utilized in the present apparatus, as indicated in Fig. 1 (right panel), in which a toothed absorber structure is arranged on the back plane of the central chamber. As the subsequent results show, the absence of absorber along the arc of the semi-circular plates does not appear to interfere noticeably with the data, e.g., standing wave modes within the chamber are not problematic as the large chamber size and the absorber along the backside sufficiently reduce these unwanted artifacts compared to the expected radiation patterns.

The radius of the circular plates sets the detector at 16" (chamber radius) from the radiating element. The combination of the coaxial antenna and the substrate set an effective aperture, which in turn determines the characteristic Fresnel length separating the propagating near-field region from the far-field region of interest. We have not performed detailed

calculations to determine the effective aperture of the antenna, but rough arguments suggest that we are safely in the far-field region where the fields are measured. The data thus far acquired confirms this, but we will consider the topic in more detail in future work.

The waveguide detector is mounted flush with the chamber (on the semicircular face) on a toothed gear stepper motor, driven by customized software that also controls the data acquisition. Microwaves are injected into the chamber via a removable coax-fed, source antenna located at the center of the circular (Fig. 1, right panel). When using the coaxial antenna, we extend the back surface absorber material across the plane wave aperture and insert the antenna through a hole in the bottom plate.

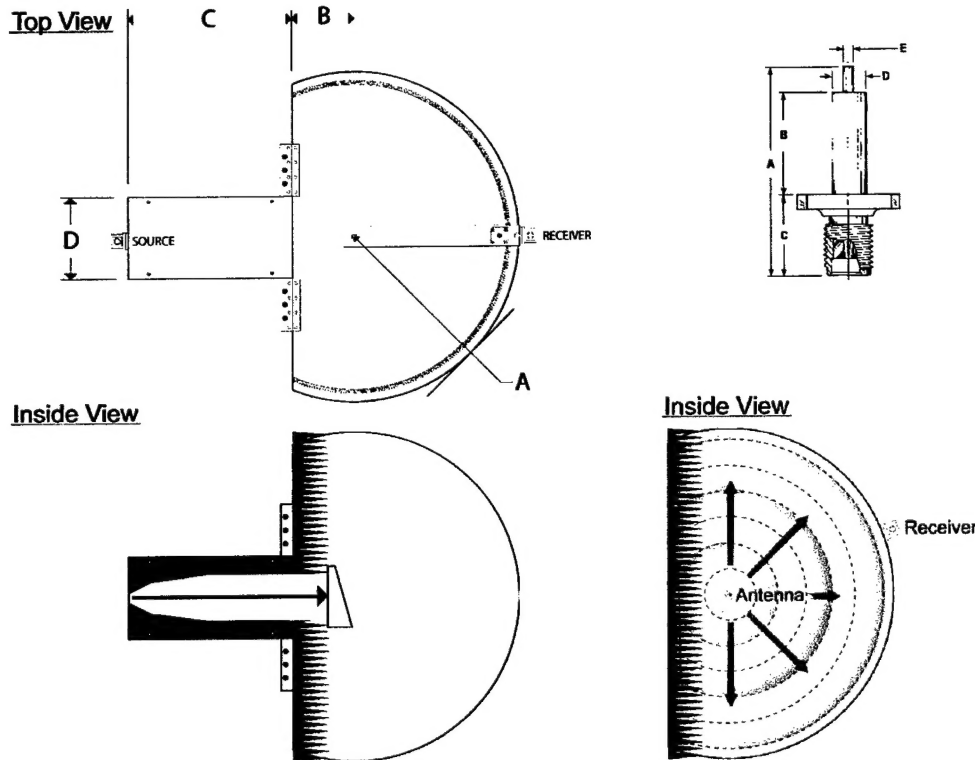


Figure 1: (Left panel) A schematic of the ARMS apparatus, in which a plane wave, launched down the rectangular wave-guide, interacts with a meta-material sample placed at the center of the circular plates ($A=16''$, $B=6''$, $C=16''$, $D=8''$, plate spacing = $0.4''$). The detector, confined to the radius by a bearing mounted arm, sweeps around circumference of the plates driven by a stepper motor. Toothed absorber (in black) is placed inside the plates to minimize unwanted reflective scattering. (Right panel) ARMS apparatus using the optional antenna source ($A=1.08''$, $B\approx 0.315''$, $C=0.375''$, $D= 0.162''$ dia, $E= 0.050''$ dia), combined with experimental backplane sample. The angle-resolved radiation pattern is determined by scanning the circumference with the detector.

Microwaves are generated and detected in the ARMS apparatus by an Agilent Vector Network Analyzer (VNA, model number 8722). While the frequency range of the VNA is 50 MHz through 40 GHz, the plate separation of the planar waveguide restricts our measurements to the frequency band 8-12 GHz, although we find acceptable data can be acquired in the range 8-16 GHz. A data acquisition program, written as a series of macros in Excel VBA (Visual Basic for Applications), controls the stepper motor (Little Step-U, TLA Microsystems, Auckland, New Zealand) that rotates the detector arm, in addition to controlling the VNA (Fig. 2).

The angular stepping motion of the detector induces vibrations in the detector arm. In order to avoid introduction of unwanted structure into the data, a delay (usually one second) is used to allow for damping of the vibrations before the control program initiates acquisition or averaging of the data.

The accuracy of the ARMS waveguide apparatus is in part determined by the flatness of the $\frac{1}{4}$ " thick aluminum plates (rolled sheet aluminum) which make up the upper and lower central chamber plates and the plates of the extended channel. As purchased, the lower central chamber plate was significantly warped. To remedy this, it was necessary to flatten the plate by mounting three 1" square aluminum straightening rods to the bottom surface. The rods were drilled with several $> \frac{1}{4}$ " through-holes, with corresponding $\frac{1}{4} \times 20$ blind tapped holes machined into the bottom of the lower aluminum plate. When the straightening rods were brought flush with the aluminum plate surface by means of tightening the $\frac{1}{4} \times 20$ machine screws, the aluminum plate became nearly flat. Starting with a machine ground $\frac{1}{4}$ " aluminum plate rather than the rolled sheet aluminum might reduce the need for straightening bars for further improved performance.

The antenna source, which in our case is the projecting pin of a coaxial panel jack receptacle (Applied Engineering Products, Model 9004-x113-000 or similar) is used to produce cylindrical waves. In keeping with the two-dimensional confined nature of the ARMS apparatus, we would ideally like to use a linear current source as the localized excitation, which would couple strictly to the lowest propagating modes in the chamber. In reality, our source protrudes into the chamber a finite distance, and produces image charges on the upper and lower plates. The resulting electromagnetic source presumably couples in a complicated manner to the higher order modes of the chamber, although none of these higher order modes propagate at frequencies below 14.8 GHz. Nevertheless, the antenna excitation we use has excellent reproducibility, and can be used to probe antenna/metamaterial interactions.

Fig. 2 shows the reproducibility of an angular scan, with the power introduced by the antenna excitation. Two scans were made, and the intensity from one scan divided by the intensity of the second scan. The reproducibility, as determined from the scatter in the measurement, corresponds to -30 dB. For antenna backplane measurements, where ~ 0.1 dB accuracy is typically needed, the ARMS chamber can provide extremely sensitive measurements.

Antenna Backplane Calculations

The solution of a line source above an infinite half-space of arbitrary material can be readily found by expanding the line source in terms of plane waves, and calculating the reflection coefficient for each plane wave. We have developed this semi-analytical method [see W. C. Chew, *Waves and Fields in Inhomogeneous Media*, (IEEE Press, New York, 1995), Section 2.2.1] in order to compare with experiments and numerical finite-element based simulations.

An example of the utility of the method is shown in Fig. 3a, where we plot the intensity versus angle of a line source next to a "perfect electric conductor," or PEC. The PEC tends to short the line source as it approaches the surface, so that the total radiated power is reduced. When the line source is $\lambda/4$ away from the surface, however, the reflected waves are constructive so that the forward gain is actually enhanced relative to the line source in free space.

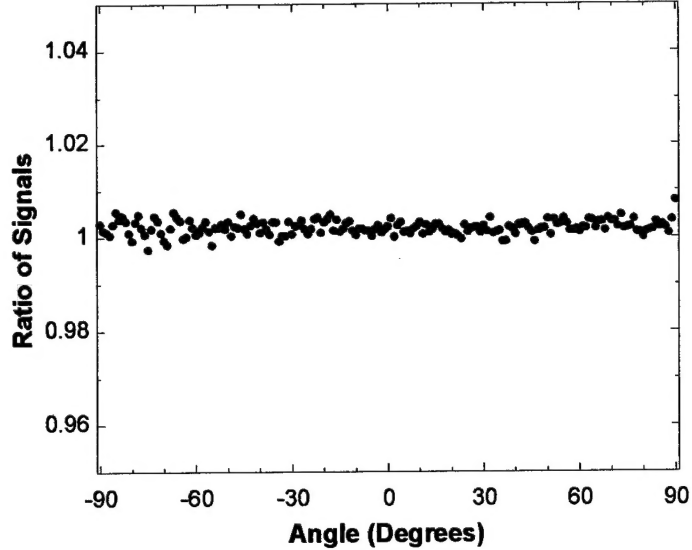


Figure 2: Experimental data which displays the reproducible, low noise angular scan of the ARMS apparatus with the center antenna source radiating without a sample backplane. The low noise ratio of two consecutive scans means that by normalizing the instrument to an empty scan, the radiation pattern from a sample backplane can be accurately measured.

The influence of material properties can be seen by comparing Fig. 3a with Fig. 3b, which shows gain curves for a line source next to a “perfect magnetic conductor,” or PMC. The PMC is not realizable in conventional materials, but provides an indication as to how materials might be engineered for useful communications applications. Note that instead of reducing the radiative power when the line source approaches the surface, the PMC actually enhances the radiative power by roughly a factor of two over a free space line source; furthermore the gain curve is flat over all angles when the line source is in direct contact with the surface. This example is illustrative, as it is not our intent to pursue PMC equivalent materials; numerous groups are working on this application, with some success. Our immediate purpose is to utilize the method to compare with measurements in the ARMS apparatus. We present these measurements in the following section. Because we will eventually be interested in the response from different types of metamaterial substrates, we have created a general code (in Mathematica) to calculate gain curves for a line source above a half-space of material characterized by arbitrary ϵ and μ tensors. Thus, we have the capability to study materials such as the indefinite media discussed in previous reports.

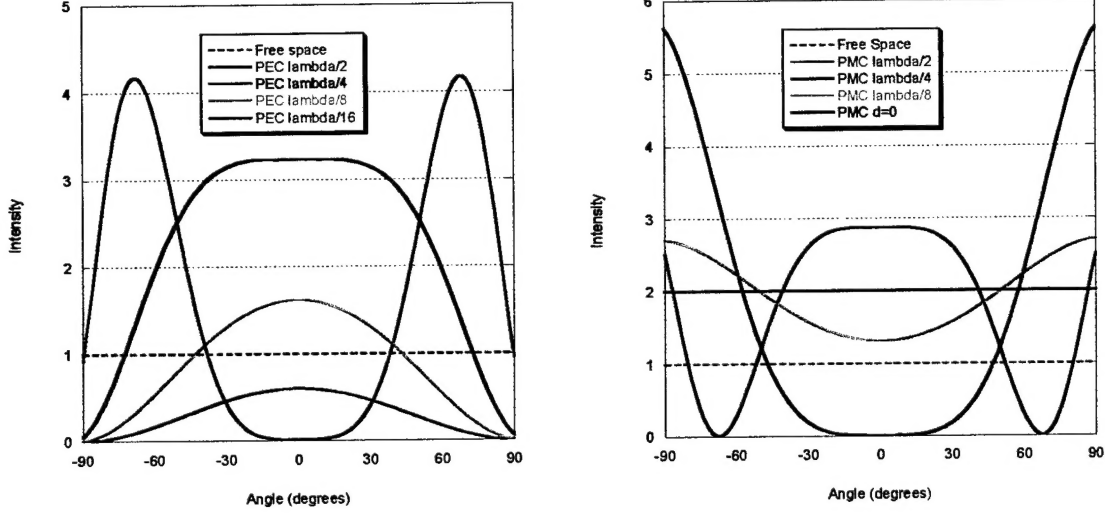


Figure 3: (a) Gain curves for a line source at varying distances from a “perfect electric conductor” (PEC). (b) Gain curves for a line source at varying distances from a “perfect magnetic conductor” (PMC).

Calibration Measurements: PEC

To determine whether our ARMS apparatus would produce reliable antenna back plane measurements, we first studied the coaxial line at varying distances (and frequencies) in front of an approximate PEC. In this case, the PEC was a rectangular aluminum slab placed inside the chamber at a fixed distance of 1.3 cm from the antenna. Rather than moving the antenna to study the distance dependence of the gain patterns, the frequency was swept from 8 to 16 GHz. The values of δ shown in the figure refer to the distance of the line source to the PEC in terms of wavelength. The three plots in Fig. 4 demonstrate quite good agreement with the semi-analytical model described above. There is some deviation from the theoretical curves, especially near the end-fire positions; this deviation may be expected as our sample is of finite extent and as the antenna we are using is significantly different from an ideal line source. Given the simplicity of the model and the actual experimental configuration, the agreement is quite acceptable.

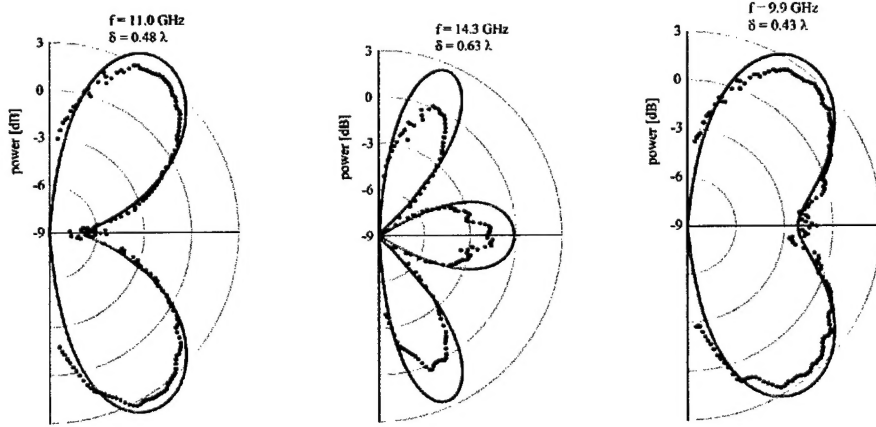


Figure 4: Gain profiles for a coaxial antenna backed by a conducting plane. The dots correspond to the measured gain, while the overlayed solid curves correspond to the gain calculated by an analytical model. (Left) Frequency of 11.0 GHz, (Middle) 14.3 GHz, and (Right) 9.9 GHz.

Preliminary Measurements on a Metamaterial Sample as Backplane

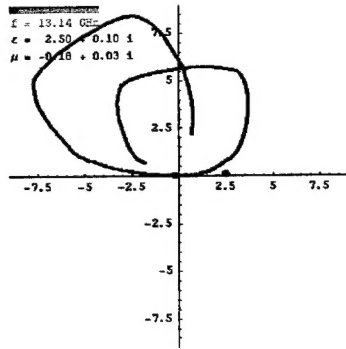
Having shown the feasibility of backplane measurements using our ARMS apparatus, our next step is to characterize metamaterial samples as antenna backplanes. This step requires a considerable effort, as the material properties of metamaterials themselves are difficult to characterize, which makes comparison with theory an even greater challenge. Nevertheless, as our final step in this reporting period, we have initial results that indeed appear very promising.

One of the simpler structures for us to consider is a metamaterial sample made only of split ring resonators (SRR). Using our established methods of analysis, we simulated an metamaterial composed of SRRs. The design consisted of SRRs in one dimension only, so that the sample was anisotropic. The effective ϵ and μ tensors of the effective medium were recovered using S-parameter inversion, as well as the effective index-of-refraction (n) and impedance (z). The latter two parameters provide the best indicators of expected performance, particularly for isotropic samples. For isotropic samples, either large or small z implies a highly reflective sample that can clearly function as a backplane. When z is of moderate value, however, the index provides a measure of the penetration depth and an indication as to how thick the sample must be to perform as a reflector plane. The SRR sample used here was not designed for any particular application other than as a test structure; our goal was to understand how closely the gain pattern from an antenna next to a fabricated metamaterial would match the gain predicted from the derived material parameters used in the semi-analytical model.

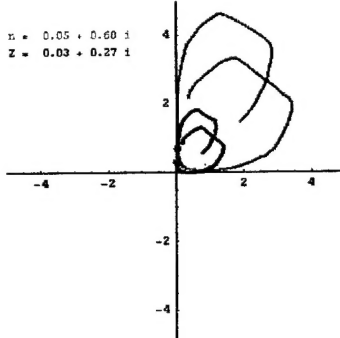
The results of the measurements are shown in Fig. 5, in which we present plots of the predicted material properties (ϵ and μ), complex index and impedance and measured gain curves for the SRR metamaterial. We have selected three frequencies at which data is presented. As a function of frequency, the material parameters trace out curves such as that shown in the leftmost two plots in the figure. Two black dots indicate the calculated values of either ϵ and μ (far left) or n and z (middle plot); using these values in the semi-analytical model of a line source next to a half-space we can derive the expected gain curve, shown as the solid green curve in Fig. 5. The measured points are also shown in the figure. These curves provide strong evidence that we can apply metamaterial as backplanes and obtain reliable and predictable results. We should caution that we have presented three of the better regions of agreement; at other frequencies we noted a greater discrepancy between predicted and measured gain.

Having established our capabilities of metamaterial design, fabrication and measurement for the purpose of antenna backplane applications, we plan to continue to on the path outlined at the beginning of this section. In particular, we will work to improve further the measured gain characteristics with that expected from the recovered material parameters from the metamaterial designs. We will evaluate the effects of finite-sized backplanes utilizing full-wave finite-element modeling. We will also analyze the gain characteristics for backplanes composed of materials whose material parameters vary throughout the volume. *This effort is an important precursor to advanced reconfigurable metamaterials.*

Calculated μ



Calculated n and z



Measured Gain

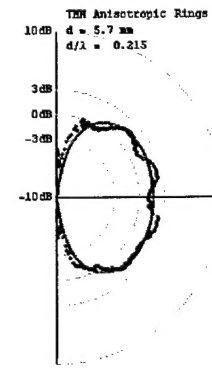
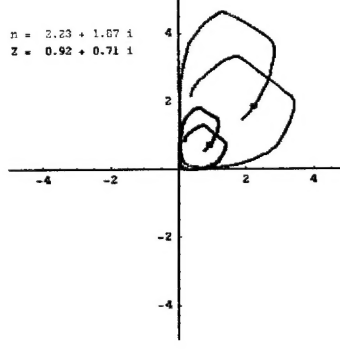
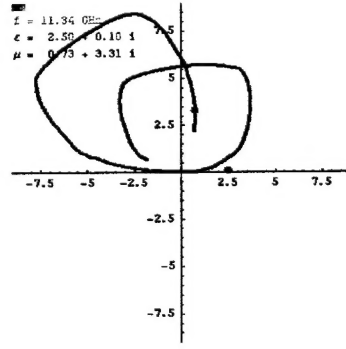
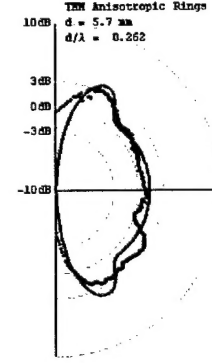
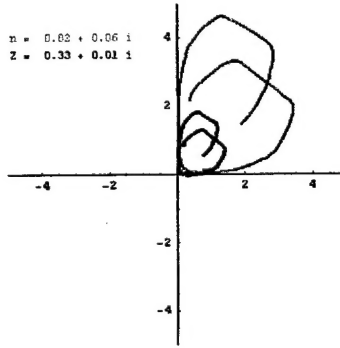
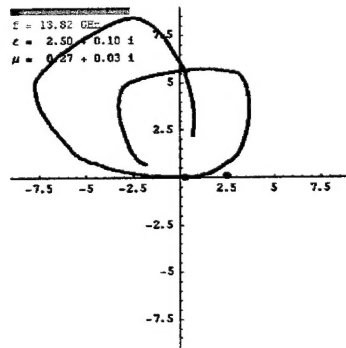
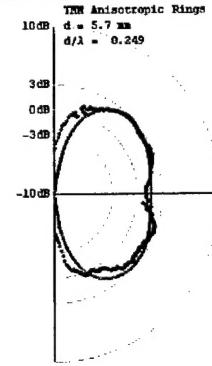


Figure 5: (left) the value of μ as a function of frequency. The vertical axis corresponds to $\text{Im}(\mu)$ while the horizontal axis corresponds to $\text{Re}(\mu)$; ϵ is approximated to have the value $2.5 + 0i$ throughout. As a function of frequency, μ traces out the curve shown in the complex plane; the two black dots indicate the values of ϵ and μ at the frequency studied. (center) We present the values of complex n and z as a function of frequency. (right) Measured (dots) and calculated (solid curve) gain curves for three frequencies (13.14 GHz, 13.82 GHz and 11.34 GHz). The lighter dots of the measured points indicate where the penetration depth is larger than our sample size, such that these points are likely to have significant error.

II. Magnetic Field Modulation of the Split Ring Resonators

It is clear that as negative index of refraction or indefinite media designs become available for applications as lenses, antenna substrates, "designer" index and surface impedance materials and other purposes, there will be a corresponding need to provide the features of signal modulation, on/off switching, directional radiation control, etc. We have suggested that since the key properties of LHM depend on the ability to incorporate specific values (of both positive and negative sign) of the effective permeability tensor, it is an optimum strategy to use magnetic fields to provide the external control. One of the simplest approaches is to place strongly paramagnetic spin materials at the centers of the SRR where their microwave fields are the strongest. While all types of magnetic materials may eventually prove useful, we have decided to initially use paramagnetic spins as being the most instructive and flexible first case to investigate.

We also have chosen to exploit electron spin resonance for the simple reason that this happens to be an area in which we have a complete range of spectrometers, ancillary equipment, and many years of direct experience designing diverse test structures and measurement techniques. In Fig. 6 we present four pictures illustrating our initial work. The large left side picture is a snapshot of one of the several magnet-electronic-cryogenic ESR stations. The top right side figure shows the end of a pair of waveguides which permit measurements of the transmission of microwaves (in the 8-12 GHz band) through a small sample placed inside. In the bottom smaller picture we see a blow up of a single SRR which is built as an inner and outer pair of "C" sections. In the right small picture we see a similar SRR coated with an appropriate paramagnetic spin material.

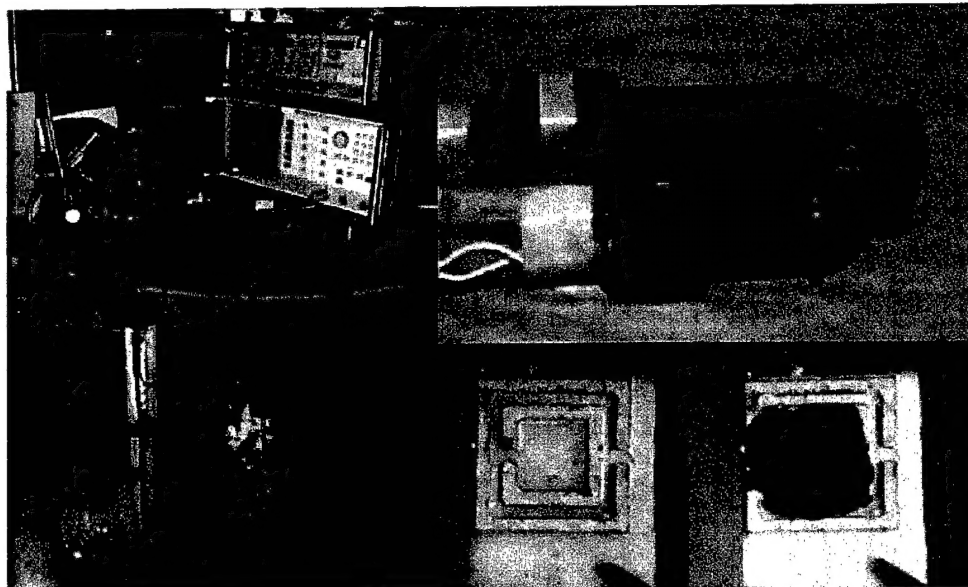


Figure 6: (left) Magnet and microwave spectrometer apparatus. (upper right) X-band microwave waveguide fittings for transmission measurements. (lower middle) A split ring resonator. (lower right) A split ring resonator loaded with DPPH.

In Fig. 7 we observe the transmitted power (curved white line) as a function of microwave frequency which is transmitted past an individual SRR appropriately oriented within the center region of the waveguide. The white dot at the center of the lowest point of curvature of the transmitted power indicates the center frequency of the actual resonance response of the SRR. In

the right side picture, we see the effect on that transmitted power when an applied dc external magnetic field is brought to the value which drives the spins into their resonance. For a frequency of 10 GHz, the resonant field is approximately 3.3 KGauss. Note that the bottom of the transmitted power curve is significantly perturbed (quantitatively by ~ 3 db). Since a typical LHM sample contains many unit cells, each of which having one (or more) SRRs, we can appreciate that we can expect significant changes in the microwave behavior of a typical LHM by applying magnetic fields.

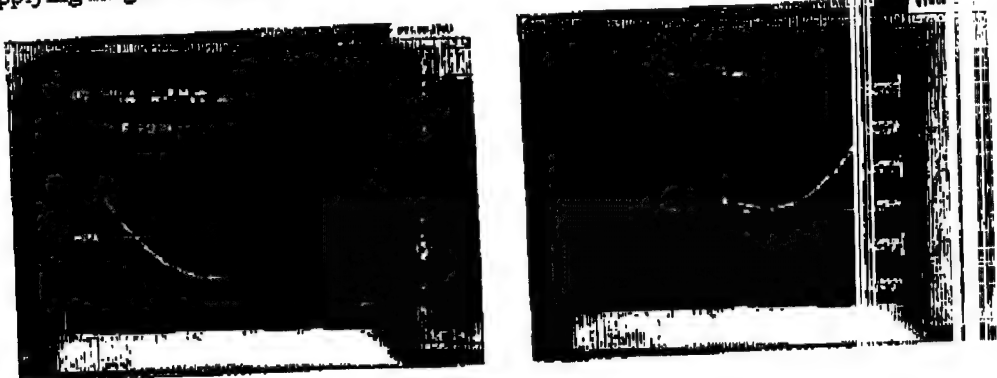


Figure 7: (Left) The lower part of the attenuated transmission region corresponding to the resonance of the single split ring loaded with DPPH (See Fig. 6, lower right). The scale is expanded to show only the lowest part of the curve. The figure is actually a photograph of the network analyzer trace. (Right) The resonance curve with a field of 3.3 KGauss applied. The resonance of the DPPH sample can be seen as a distortion in the resonance of the split ring resonator.

The usual bag of tricks will now be explored: (i) one can orient the dc field so as to activate one or more of the SRRs within a designed unit cell. (ii) one can produce linear modulation in major attenuation for on/off switching, and (iii) since the ESR linewidth can be made a very small fraction of the dc value, large modulations can be achieved with relatively small amounts of signal control power.

The transition to full sized samples can involve the selective spin "loading" of a selected set of SRRs, or the entire group. Experiments are in process of determining efficient ways of applying the spin "dots", since it must be appreciated that our current typical unit cell dimension is 1.0 Ghz and is 2.5 mm, and the inner ring diameter is ~1 mm! We have designed an entire set of tests and samples to be used, and of course since we can readily go to cryogenic temperatures, we will gain by the factor of improvement in kT since the spins are paramagnetic.

BEST AVAILABLE COPY

Electromagnetic Wave Propagation in Media with Indefinite Permittivity and Permeability Tensors

D. R. Smith and D. Schurig

Physics Department, University of California-San Diego, La Jolla, California 92093

(Received 25 June 2002; published 21 February 2003)

We study the behavior of wave propagation in materials for which not all of the principal elements of the permeability and permittivity tensors have the same sign. We find that a wide variety of effects can be realized in such media, including negative refraction, near-field focusing, and high impedance surface reflection. In particular, a bilayer of these materials can transfer a field distribution from one side to the other, including near fields, without requiring internal exponentially growing waves.

DOI: 10.1103/PhysRevLett.90.077405

PACS numbers: 78.20.Ci, 42.25.-p, 78.67.-n, 84.40.-x

The range of available electromagnetic material properties has been broadened by recent developments in structured media, notably photonic band gap materials and metamaterials. These media have allowed the realization of solutions to Maxwell's equations not available in naturally occurring materials, fueling the discovery of new physical phenomena and the development of devices.

Photonic crystal effects typically occur when the wavelength is on the same order or smaller than the lattice constant of the crystal. Metamaterials, on the other hand, have unit cell dimensions much smaller than the wavelength of interest. A homogenization process, not unlike that applied in Ref. [1], can allow the otherwise complicated composite medium to be described conveniently by a permittivity tensor (ϵ) and a permeability tensor (μ), rather than by band diagrams.

In 2000, it was shown experimentally that a metamaterial composed of periodically positioned scattering elements, all conductors, could be interpreted as having simultaneously a negative effective ϵ and a negative effective μ [2]. A medium with simultaneously isotropic and negative ϵ and μ supports propagating solutions whose phase and group velocities are antiparallel; equivalently, such a material can be rigorously described as having a negative index of refraction [3,4]. An experimental observation of negative refraction was reported using a metamaterial composed of wires and split ring resonators deposited lithographically on circuit board material [5].

The prospect of negative refractive materials has generated considerable interest, as this simply stated material condition suggests the possibility of extraordinary wave propagation phenomena, including near-field focusing [6]. So remarkable have been the claims surrounding negative refraction, that some researchers have been prompted to examine critically the achievability of negative refraction in existing metamaterials [7,8]. While such concerns might appear relevant in the context of frequency-dispersive materials, the interpretation of these structured materials as negative refractive has been entirely consis-

tent with all aspects of reported experimental data [2,5], as well as with numerical simulations of both monochromatic and modulated beams [9,10]. For the purposes of this Letter, we thus assume that the descriptions presented here will be applicable to real materials, although the extent to which this is true remains a topic of active pursuit [11].

Lindell *et al.* [12] have shown that the property of negative refraction is not confined to materials with negative definite ϵ and μ tensors, but can be expected to occur in certain classes of uniaxially anisotropic media. We explore here the general electromagnetic solutions associated with these anisotropic media, focusing on combinations of such media that provide access to the underlying properties. While there is a substantial reflection coefficient for non-normal waves incident on an anisotropic material from an isotropic material (or free space), due to the difference in dispersion properties of the two materials, a highly transmissive composite structure composed of layers of positively and negatively refracting anisotropic materials can be formed. As a specific example, we present an analysis of a compensated bilayer that produces subwavelength near-field focusing, but mitigates the thickness and loss limitations of the isotropic "perfect lens."

To simplify the proceeding analysis, we assume a linear material with ϵ and μ tensors that are simultaneously diagonalizable,

$$\epsilon = \begin{pmatrix} \epsilon_x & 0 & 0 \\ 0 & \epsilon_y & 0 \\ 0 & 0 & \epsilon_z \end{pmatrix}, \quad \mu = \begin{pmatrix} \mu_x & 0 & 0 \\ 0 & \mu_y & 0 \\ 0 & 0 & \mu_z \end{pmatrix}. \quad (1)$$

Metamaterials can be readily constructed that closely approximate these ϵ and μ tensors, with elements of either algebraic sign. In fact, the scattering elements comprising the metamaterials used to demonstrate negative refraction [5,13] are appropriate building blocks for the classes of materials to be discussed here (see Fig. 1).

We apply the term *indefinite* to anisotropic media in which not all of the principal components of the ϵ and μ

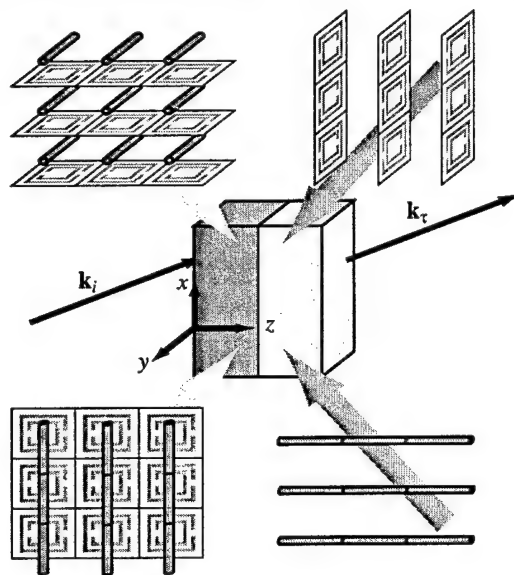


FIG. 1. A bilayer composed of indefinite media implemented using split ring resonators and straight wires. The structures in the top of the figure implement *never cutoff* media for electric y polarization. Top left is negative refracting and top right is positive refracting. The structures in the bottom of the figure do the same for magnetic y polarization.

tensors have the same sign. We will consider here layered media with surfaces normal to one of the principal axes, which we define to be the z axis. We assume in our analysis a plane wave with the electric field polarized along the y axis having the specific form

$$\mathbf{E} = \hat{\mathbf{y}} e^{i(k_x x + k_z z - \omega t)}, \quad (2)$$

though it is generally possible to construct media that are polarization independent, or that exhibit different classes of behavior for different polarizations. The plane wave solutions specified by Eq. 2 satisfy the dispersion relation

$$k_z^2 = \epsilon_y \mu_x \frac{\omega^2}{c^2} - \frac{\mu_x}{\mu_z} k_x^2. \quad (3)$$

Since we have no x or y oriented boundaries or interfaces, real exponential solutions, which result in field divergence when unbounded, are not allowed in those directions. Furthermore, k_x is restricted to be real. Also, since k_x represents a variation transverse to the surfaces of our layered media, it is conserved across the layers, and naturally parametrizes the solutions.

In the absence of losses, the sign of k_z^2 can be used to distinguish the nature of the plane wave solutions. $k_z^2 > 0$ corresponds to real valued k_z and propagating solutions. $k_z^2 < 0$ corresponds to imaginary k_z and exponentially growing or decaying (evanescent) solutions. When $\epsilon_y \mu_z > 0$, there will be a value of k_x for which $k_z^2 = 0$. This value, which we denote k_c , is the cutoff wave vector separating propagating from evanescent solutions. From

Eq. (3), this value is $k_c = \frac{\omega}{c} \sqrt{\epsilon_y \mu_z}$. We identify four classes of media based on their cutoff properties:

	Media conditions	Propagation
Cutoff	$\epsilon_y \mu_x > 0$	$\mu_x / \mu_z > 0$
Anti-cutoff	$\epsilon_y \mu_x < 0$	$\mu_x / \mu_z < 0$
Never cutoff	$\epsilon_y \mu_x > 0$	$\mu_x / \mu_z < 0$
Always cutoff	$\epsilon_y \mu_x < 0$	$\mu_x / \mu_z > 0$
		All real k_x
		No real k_x

Note the analysis presented here is carried out at constant frequency, and that the term *cutoff* always refers to the transverse component of the wave vector, k_x , not the frequency, ω . Isofrequency contours, $\omega(\mathbf{k}) = \text{const}$, show the required relationship between k_x and k_z for plane wave solutions (Fig. 2).

The general relationship between the directions of energy and phase velocity for waves propagating within an indefinite medium can be found by calculating the group velocity, $\mathbf{v}_g \equiv \nabla_{\mathbf{k}} \omega(\mathbf{k})$. \mathbf{v}_g specifies the direction of energy flow for the plane wave, and is not necessarily parallel to the wave vector. $\nabla_{\mathbf{k}} \omega(\mathbf{k})$ must lie normal to the isofrequency contour, $\omega(\mathbf{k}) = \text{const}$, as illustrated in Fig. 2. Calculation of $\nabla_{\mathbf{k}} \omega(\mathbf{k})$ from the dispersion relation, Eq. (3), determines which of the two possible normal directions yields increasing ω and is thus the correct group velocity direction. Performing an implicit differentiation of Eq. (3) leads to a result for the gradient that does not require square root branch selection, removing any sign confusion. To obtain physically meaningful results, a causal, dispersive response function, $\xi(\omega)$, must be used to represent the negative components of ϵ and μ , since these components are necessarily dispersive [14]. The response function should assume the desired (negative) value at the operating frequency, and satisfy the causality requirement that $\partial(\xi\omega)/\partial\omega \geq 1$ [4,14]. Combining this with the derivative of Eq. (3) determines which of the two possible normal directions applies, without specifying a specific functional form for the response function. Figure 2 relates the direction of the group velocity to a given material property tensor sign structure.

Having calculated the energy flow direction, we can determine the refraction behavior of indefinite media by applying two rules: (i) The transverse component of the wave vector, k_x , is conserved across the interface, and (ii) energy carried into the interface from free space must be carried away from the interface inside the media; i.e., the normal component of the group velocity, v_{gz} , must have the same sign on both sides of the interface. Figure 2 shows typical refraction diagrams for the three types of media that support propagation.

To illustrate the unique possibilities associated with indefinite media, we recall that a motivating factor in recent metamaterials research has been the project of near-field focusing. A planar slab with isotropic $\epsilon = \mu = -1$ can act as a lens with resolution well beyond the

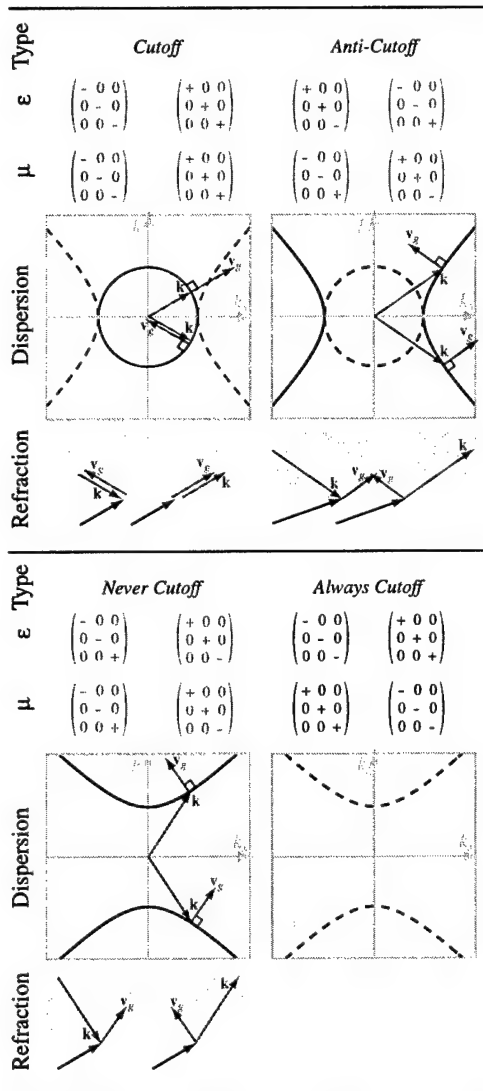


FIG. 2 (color). Material property tensor forms, dispersion plot, and refraction diagram for four classes of media. Each of these media has two subtypes: one positive (blue) and one negative (red) refracting, with the exception that *always cutoff* media do not support propagation and refraction. The dispersion plot shows the relationship between the components of the wave vector at fixed frequency. k_x (horizontal axis) is always real, k_z (vertical axis) can be real (solid line) or imaginary (dashed line). (The closed contours are shown circular, but can more generally be elliptical.) The same wave vector and group velocity vectors are shown in the dispersion plot and the refraction diagram. v_g shows direction only. The shaded diagonal tensor elements are responsible for the shown behavior for electric y polarization, the unshaded diagonal elements for magnetic y polarization.

diffraction limit [6]. It is difficult, however, to realize significant subwavelength resolution with an isotropic negative index material, as the required exponential growth of the large k_x field components across the nega-

tive index lens leads to extremely large field ratios. Sensitivity to material loss and other factors can significantly limit the subwavelength resolution.

By combining positive and negative refracting layers of *never cutoff* indefinite media, we can produce a compensated bilayer that accomplishes near-field focusing in a similar manner to the perfect lens, but with significant advantages. Figure 2 indicates that, for the same incident plane wave, the z component of the transmitted wave vector is of opposite sign for these two materials. Combining appropriate lengths of these materials results in a composite indefinite medium with unit transfer function. We can see this quantitatively by computing the general expression for the transfer function of a bilayer using standard boundary matching techniques [15],

$$T = 8[e^{i(\phi+\psi)}(1-Z_0)(1+Z_1)(1-Z_2) + e^{i(\phi-\psi)}(1-Z_0)(1-Z_1)(1+Z_2) + e^{i(-\phi+\psi)}(1+Z_0)(1-Z_1)(1-Z_2) + e^{i(-\phi-\psi)}(1+Z_0)(1+Z_1)(1+Z_2)]^{-1}. \quad (4)$$

The relative effective impedances are defined as

$$Z_0 = \frac{q_{z1}}{\mu_{x1}k_z}, \quad Z_1 = \frac{\mu_{x1}q_{z2}}{\mu_{x2}q_{z1}}, \quad Z_2 = \mu_{x2}\frac{k_z}{q_{z2}}, \quad (5)$$

where \mathbf{k} , \mathbf{q}_1 , and \mathbf{q}_2 are the wave vectors in vacuum and the first and second layers of the bilayer, respectively. The individual layer phase advance angles are defined as $\phi = q_{z1}L_1$ and $\psi = q_{z2}L_2$, where L_1 is the thickness of the first layer and L_2 is the thickness of the second layer. If the signs of q_{z1} and q_{z2} are opposite as mentioned above, the phase advances across the two layers can be made equal and opposite, $\phi + \psi = 0$. If we further require that the two layers are impedance matched to each other, $Z_1 = 1$, then Eq. (4) reduces to $T = 1$ (the transfer function of free space is $T = e^{ik_z(L_1+L_2)}$). In the absence of loss, the material properties can be chosen so that this occurs for all values of the transverse wave vector, k_x . Transfer functions with varying amounts of loss added are shown in Fig. 3.

A proposed implementation is shown in Fig. 1. The elements shown in the top and bottom of the figure will implement media that focuses electric y -polarized and magnetic y -polarized waves, respectively. Combining the two structures forms a bilayer that is x - y isotropic due to the symmetry of the combined lattice. This symmetry and the property $\mu = \epsilon$ yield polarization independence. The materials are formed from split ring resonators and wires with numerically and experimentally confirmed effective material properties [5]. Each split ring resonator orientation implements negative permeability along a single axis, as does each wire orientation for negative permittivity.

While compensated bilayers of indefinite media exhibit reduced impedance mismatch to free space and

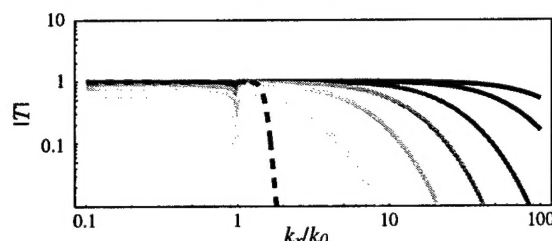


FIG. 3. Magnitude of the transfer function vs transverse wave vector, k_x , for a bilayer composed of positive and negative refracting *never cutoff* media. Material property elements are of unit magnitude and layers of equal thickness, λ . A loss producing imaginary part has been added to each diagonal component of ϵ and μ , with values 0.001, 0.002, 0.005, 0.01, 0.02, 0.05, and 0.1 for the darkest to the lightest curve. For comparison, a single layer, isotropic near field lens is shown dashed. The single layer has thickness λ , and $\epsilon = \mu = -1 + 0.001i$.

high transmission, uncompensated semi-infinite indefinite media exhibit unique high reflection properties. Aside from *cutoff* materials, other classes of indefinite media have a reflection coefficient amplitude near unity for incident propagating waves. The phase of the reflection coefficient, however, varies, as illustrated here for positive refracting *anti-cutoff* media. The reflection coefficient for electric y polarization is given by

$$\rho = \frac{\mu_x k_z - q_z}{\mu_x k_z + q_z}, \quad (6)$$

where \mathbf{k} and \mathbf{q} are the wave vectors in vacuum and the media, respectively. For unit magnitude *anti-cutoff* material we have, from Eq. (3),

$$q_z^2 = -\frac{\omega^2}{c^2} + k_x^2 = -k_z^2. \quad (7)$$

Thus, $q_z = \pm ik_z$. The correct sign for positive refracting media, +, is determined by the requirement that the fields must not diverge in the domain of the solution. We then have

$$\rho = \frac{1-i}{1+i} = -i. \quad (8)$$

The magnitude of the reflection coefficient is unity, with a phase of -90° for propagating modes of *all* incident angles. An electric dipole antenna placed $\lambda/8$ away from the surface would thus be enhanced by interaction with this "mirror" surface. Customized reflecting surfaces are of practical interest, as they enhance the efficiency of nearby antennas, while at the same time providing shielding [16,17]. Furthermore, an interface between unit *cutoff* and *anti-cutoff* media has no solutions that are simultaneously evanescent on both sides, i.e., surface modes (Fig. 2). In many communications applications,

the energy lost to the excitation of surface modes is undesirable, as it represents loss of signal power.

In conclusion, we have begun to explore the properties of media with indefinite ϵ and μ tensors. Consideration of layered structures has led to useful and interesting reflection and refraction behavior, including a new mechanism for subdiffraction focusing. We note that neither the analysis nor the fabrication of these media is complicated, and thus anticipate other researchers will quickly assimilate the principles and design structures with unique and technologically relevant properties.

We thank Claudio Parazzoli (Phantom Works, Boeing) for motivating this work. This work was supported by DARPA (Contract No. 972-01-2-0016), ONR (Contract No. N00014-00-1-0632), and AFOSR (Contract No. F49620-01-1-0440).

Note added.—While preparing this manuscript, we learned that a focal spot of $\lambda/25$ was experimentally achieved in a lumped circuit analog of the bilayer geometry [18].

- [1] P. Halevi, A. A. Krokkin, and J. Arriaga, Phys. Rev. Lett. **82**, 719 (1999).
- [2] D. R. Smith *et al.*, Phys. Rev. Lett. **84**, 4184 (2000).
- [3] V. G. Veselago, Sov. Phys. Usp. **10**, 509 (1968).
- [4] D. R. Smith and N. Kroll, Phys. Rev. Lett. **85**, 3966 (2000).
- [5] R. A. Shelby, D. R. Smith, and S. Schultz, Science **292**, 79 (2001).
- [6] J. B. Pendry, Phys. Rev. Lett. **85**, 3966 (2000).
- [7] P. M. Valanju, R. M. Walser, and A. P. Valanju, Phys. Rev. Lett. **88**, 187401 (2002).
- [8] N. Garcia and M. Nieto-Vesperinas, Phys. Rev. Lett. **88**, 207403 (2002).
- [9] J. A. Kong, B. Wu, and Y. Zhang, Appl. Phys. Lett. **80**, 2084 (2002).
- [10] D. R. Smith, D. Schurig, and J. B. Pendry, Appl. Phys. Lett. **81**, 2713 (2002).
- [11] R. Ruppin, Phys. Lett. A **299**, 309 (2002).
- [12] I. V. Lindell, S. A. Tretyakov, K. I. Nikoskinen, and S. Ilvonen, Microw. Opt. Technol. Lett. **31**, 129 (2001).
- [13] D. R. Smith, S. Schultz, P. Markos, and C. M. Soukoulis, Phys. Rev. B **65**, 195104 (2002).
- [14] L. D. Landau, E. M. Lifshitz, and L. P. Pitaevskii, in *Electrodynamics of Continuous Media* (Pergamon, New York, 1984), Chap. X.
- [15] A. Yariv, *Optical Waves in Crystals: Propagation and Control of Laser Radiation* (Wiley, New York, 1984).
- [16] D. Sievenpiper *et al.*, IEEE Trans. Microwave Theory Tech. **47**, 2059 (1999).
- [17] K.-P. Ma, Y. Qian, and T. Itoh, IEEE Trans. Microwave Theory Tech. **47**, 1509 (1999).
- [18] K. G. Balmain, A. A. E. Luttgen, and P. C. Kremer, IEEE Antennas Wireless Propag. Lett. **1**, 146 (2002).

Limitations on subdiffraction imaging with a negative refractive index slab

David R. Smith,^{a)} David Schurig, Marshall Rosenbluth, and Sheldon Schultz
Department of Physics, University of California, San Diego, 9500 Gilman Drive, La Jolla, California 92093-0319

S. Anantha Ramakrishna and John B. Pendry
The Blackett Laboratory, Imperial College, Prince Consort Road, London, SW7 2BZ

(Received 12 November 2002; accepted 3 January 2003)

A planar slab of material, for which both the permittivity and permeability have the values of -1 , can bring not only the propagating fields associated with a source to a focus, but can also refocus the nonpropagating near fields, thereby achieving resolution beyond the diffraction limit. We study the sensitivity of this subwavelength focus to the slab material properties and periodicity, and note the connection to slab surface plasmon modes. We conclude that significant subwavelength resolution is achievable with a single negative index slab, but only over a restrictive range of parameters. © 2003 American Institute of Physics. [DOI: 10.1063/1.1554779]

A wave incident on the interface between two materials whose indices of refraction are of opposite sign will undergo *negative refraction*. This recently appreciated propagation phenomenon has been predicted to lead to numerous interesting optical phenomena, including a superfocusing effect. Veselago showed theoretically that a planar slab with index of $n = -1$ could focus the rays from a nearby electromagnetic source to an image on the opposite side of the slab.¹ In a more recent analysis,² it was shown that in addition to the far-field components associated with a source being brought to a focus by the slab, the nonpropagating near-field components could also be recovered in the image. It was, therefore, proposed that the image created by a planar slab could, in principle, contain *all* of the information associated with the source object, thereby achieving resolution well beyond that of the diffraction limit. For this reason, the slab was described as a *perfect lens*. We maintain this description here, referring specifically to a planar slab of continuous material with $\mu = -1$ and $\epsilon = -1$ (no losses) as a perfect lens.

The resolution enhancement associated with the perfect lens was a surprising result, stimulated by the experimental demonstration³ of a *left-handed* material at microwave frequencies, for which $\epsilon < 0$ and $\mu < 0$. However, far from being a continuous material, the measured sample was comprised of two interlaced periodic arrays of copper elements, one array being composed of split ring resonators,⁴ and the other, wires.⁵

The values of the electromagnetic parameters and the spatial periodicity render the experimental sample distinct from the idealized perfect lens. The question then arises as to whether or not focusing beyond the diffraction limit can actually be observed using any practically obtained or fabricated material, or even can be simulated using standard numerical methods (e.g., finite difference or finite element) which inevitably approximate the ideal situation. We explore the inherent limitations associated with realizable materials, and the expected impact on the focusing properties of a slab.

The planar geometry we consider here allows a straight-

forward analysis to be implemented, as was used in Ref. 2. The fields from an arbitrary electromagnetic source are expanded in a Fourier series over homogeneous and inhomogeneous plane waves. The influence of the slab on each plane wave component can easily be determined by a standard transfer matrix technique. Restricting the field variation to one transverse direction, with the electric field having *S* polarization, we find the field expansion

$$\mathbf{E}(x, z, t) = \sum_{k_x} E(k_x) \exp(ik_z z + ik_x x - i\omega t) \hat{\mathbf{y}}, \quad (1)$$

where k_z and k_x are the components of the wave vector normal to and parallel to the slab, respectively. Outside the slab, the wave equation leads to the usual dispersion relation relating the frequency ω and the components of the wave vector, or $k_z = \sqrt{\omega^2/c^2 - k_x^2}$. Those modes for which $|k_x| < \omega/c$ are propagating, while those for which $|k_x| > \omega/c$ decay evanescently along the propagation direction (z). As was shown in Ref. 2, *it is the latter inhomogeneous modes that are responsible for image resolution beyond the diffraction limit*. The ability to recover these components in an image is what distinguishes a negative index structure from all other positive index materials.

For each plane wave component, we can determine a transfer function, defined as the ratio of the field at the image plane to that at the object plane. For an *S*-polarized plane wave incident on a slab of thickness d and arbitrary values of ϵ and μ , the transfer function has the form

$$\tau_S = e^{ik_z d} \left\{ \begin{array}{l} e^{q_z d} \left[\frac{1}{2} + \frac{1}{4} \left(\frac{\mu k_z}{q_z} + \frac{q_z}{\mu k_z} \right) \right] \\ + e^{-q_z d} \left[\frac{1}{2} - \frac{1}{4} \left(\frac{\mu k_z}{q_z} + \frac{q_z}{\mu k_z} \right) \right] \end{array} \right\}^{-1}, \quad (2)$$

where we have now defined $q_z = \sqrt{k_x^2 - \epsilon \mu \omega^2/c^2}$, and redefined $k_z = \sqrt{k_x^2 - \omega^2/c^2}$. The expression for *P*-polarized waves is similar to Eq. (2), with the explicitly appearing μ replaced by ϵ . We apply all of our arguments to the *S*-polarization terms in this letter, as the results for *P* polarization follow trivially.

^{a)}Electronic mail: drs@sdss.ucsd.edu

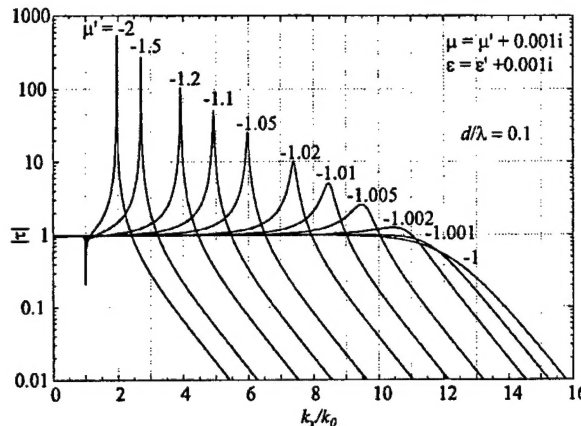


FIG. 1. Transfer function for a left-handed slab. For the perfect lens, the transfer function would be unity for all k_x . However, the deviation of either the real or imaginary part of μ limits the range of k_x , so that the slab acts as a low-pass filter. The losses, inherent to left-handed materials, also remove the singularities that appear in the transfer function.

When μ is positive, the first term in brackets will dominate the behavior of the transmitted wave for sufficiently large d and $|k_x| > \omega/c$, with the evanescent components decaying exponentially through the slab. When both ϵ and μ are equal to -1 , however, the normally dominant solution vanishes, and $\tau_s = 1$ for every component from the source field—homogeneous or inhomogeneous, thus, exactly reproducing the source field in the image plane. But the balance is delicate; any deviation from the perfect lens condition, however small, will result in an imperfect image that degrades exponentially with slab thickness d , until the usual diffraction limit is reached. This sensitivity has been noted by other researchers.^{6,7}

The effect on the image of deviations from the perfect lens condition for a given slab thickness can be estimated by determining those values of parameters which cause the two terms in Eq. (2) in brackets to be roughly equivalent. For small deviations from the perfect lens condition, we can find an approximate expression for the resolution of the slab. For $\epsilon = -1$ and $\mu = -1 + \delta\mu$, the two terms in the denominator of Eq. (2) are of approximately the same magnitude when $2k_z d = -\ln |(\delta\mu/2)^2|$. Assuming that this limit occurs when the value of k_x is large, we have $|q_z| \sim |k_z| \sim |k_x|$, and we can replace q_z with k_x . At the maximum k_x , the minimum resolvable feature will be on the scale of $\lambda_{\min} = 2\pi/k_x$. We, thus, find the resolution enhancement, $R = k_x/k_0$, of the lens as a function of small deviations in the permeability is

$$R = \frac{\lambda}{\lambda_{\min}} = -\frac{1}{2\pi} \ln \left| \frac{\delta\mu}{2} \right| \frac{\lambda}{d}. \quad (3)$$

The validity of this approximate expression can be seen by comparison with Fig. 1. For example, for a deviation of $\delta\mu = 0.005$ and $\lambda/d = 10$, the numerically computed transfer function in Fig. 1 shows that the range of k_x values near unity is approximately up to $k_x \sim 10k_0$; Eq. (3) predicts $R \sim 9.5$.

The dependence of the resolution enhancement R on the deviation from the perfect lens condition is critical. The ratio λ/d (wavelength to slab length) dominates the resolution, the logarithm term being a relatively weakly varying function.

For example, if $\lambda/d = 1.5$, we find that to achieve an R of 10, $\delta\mu$ must be no greater than $\sim 6 \times 10^{-19}$! However, for $\lambda/d = 10$, $\delta\mu$ can vary by as much as ~ 0.002 to achieve the same resolution enhancement. Deviations in either the real or the imaginary part of the permeability will result in the same resolution. The effect of varying ϵ (for S polarization) is much smaller than that associated with μ , and we do not discuss the effects of this variation further.

The transfer function has poles that occur when:

$$\tanh\left(\frac{q_z d}{2}\right) = -\frac{\mu k_z}{q_z} \quad \text{or} \quad \coth\left(\frac{q_z d}{2}\right) = -\frac{\mu k_z}{q_z}. \quad (4)$$

Equation (4) corresponds to the dispersion relations for slab plasmon polaritons.^{8,9} For certain values of k_x , these dispersion relations are satisfied, and resonant surface modes can exist on the slab. The direct excitation of these surface modes for imaging applications is undesirable, as the corresponding k_x components will be disproportionately represented in the image. Yet, the existence of these resonances is essential, as the recovery of the evanescent modes can be seen as the result of driving the surface plasmon far off resonance. The appearance of resonances can be seen in Fig. (1), which shows the transfer function as a function of k_x .

While losses severely limit the obtainable resolution of the focus for a negative index slab, periodicity, as exists for example in structured *metamaterials*³ or in the sampling associated with finite-difference simulations, also imposes a significant resolution limitation. The effect of periodicity is minimal for propagating plane waves whose wavelength is much larger than the repeated unit-cell size; however, periodicity has a significant effect on the recovery of the non-propagating components having large transverse wave number.

We can introduce periodicity into this analysis in an approximate manner. The wave equation in a medium, assuming that \mathbf{E} is polarized in the y direction, is

$$\frac{\partial^2 E_y}{\partial x^2} + \frac{\omega^2}{c^2} n^2(x) E_y = q_z^2 E_y. \quad (5)$$

We have assumed that the periodic variation in the index is only in the transverse (x) direction. Under these assumptions, $n^2(x) = n^2(x+a)$, where a is the repeat distance.

Due to the periodicity in $n^2(x)$, Eq. (5) in Fourier space will involve sums over reciprocal lattice vectors $g_n = 2n\pi/a$. However, to obtain a rough estimate of the limitation that periodicity imposes on the resolution enhancement, we solve Eq. (5) for an index having the form

$$n^2(x) = 1 + 2\Delta \sin \frac{2\pi x}{a}. \quad (6)$$

Using this form in Eq. (5) and assuming the periodic modulation is sufficiently weak that only two bands need be considered, we find the modified dispersion relation by evaluating the determinant

$$\begin{vmatrix} k_0^2 - k_x^2 - q_z^2 & k_0^2 \Delta^2 \\ k_0^2 \Delta^2 & k_0^2 - (k_x - g)^2 - q_z^2 \end{vmatrix} = 0, \quad (7)$$

where $g = 2\pi/a$ and $k_0 = \omega/c$. When $\Delta \ll 1$, the bands only weakly couple, and we ignore the effects of higher mode

excitation to find an expression for q_z . When the two terms in the denominator of Eq. (2) are roughly equal, we then have the condition

$$q_z d = -\ln \left| \frac{1}{2} \frac{k_0^2 \Delta^2}{k_z^2} \right| + \sinh^{-1} \left| \frac{g^2 - k_x^2}{2k_0^2 \Delta^2} \right|. \quad (8)$$

In the limit $k_0 \Delta / g \ll 1$, the resolution enhancement is approximately

$$R \equiv \frac{\lambda}{\lambda_{\min}} = \frac{1}{2\pi} \ln \left(\frac{\lambda^2}{a^2 \Delta^4} \right) \frac{\lambda}{d}. \quad (9)$$

A similar resolution enhancement limit to that obtained by a variation in material parameter is thus imposed by the introduction of periodic modulation. Similar to Eq. (6), the effects of periodicity enter logarithmically, and again lead to a critical dependence. As an example, an R of 10 for a slab with $\lambda/d=10$ and $\Delta \sim 1$ requires a periodicity of $\sim \lambda/20$. While admittedly of limited quantitative use, Eq. (9) shows that the inherent periodicity in metamaterials will impose a limitation on the resolution of the lens. This same limitation will result also from numerical methods that model a continuous material by evaluating the fields at a finite number of sampling points periodically spaced. This limitation has undoubtedly complicated numerical attempts to observe the superfocusing effect.¹⁰ A more recent numerical study has concluded that, within the parameter range determined from Eq. (6) and with a fine enough discretization grid, enhanced resolution can indeed be observed in finite-difference calculations.¹¹

It should be noted that we have applied a definition for resolution in this work that may not be appropriate for all

applications. For instance, calculations (not shown) suggest that the excitation of surface slab plasmons leads to a broad background in the image plane, with the subwavelength features superposed. However, for certain applications, the subwavelength information obtained from such an image may be of value.

Our conclusion from this analysis indicates that the perfect lens effect exists for a fairly restricted region of parameter space. Yet, demanding as these specifications are, achieving subwavelength resolution is possible with current technologies. Negative refractive indices have been demonstrated in structured metamaterials, and such materials can be engineered to have tunable material parameters so as to achieve the optimal conditions. Losses can be minimized in structures utilizing superconducting or active elements.

This work was supported under by DARPA through a grant from ONR (Contract No. N00014-00-1-0632) and AFOSR (Grant No. F49620-01-1-0440). The authors thank Dr. P. M. Platzman (Lucent) for valuable discussions.

- ¹V. G. Veselago, Sov. Phys. Usp. **10**, 509 (1968).
- ²J. B. Pendry, Phys. Rev. Lett. **85**, 3966 (2000).
- ³R. A. Shelby, D. R. Smith, and S. Schultz, Science **292**, 77 (2001).
- ⁴J. B. Pendry, A. J. Holden, D. J. Robbins, and W. J. Stewart, IEEE Trans. Microwave Theory Tech. **47**, 2075 (1999).
- ⁵J. B. Pendry, A. J. Holden, W. J. Stewart, and I. Youngs, Phys. Rev. Lett. **76**, 4773 (1996).
- ⁶J. T. Shen and P. M. Platzman, Appl. Phys. Lett. **80**, 3286 (2002).
- ⁷N. Garcia and M. Nieto-Vesperinas, Phys. Rev. Lett. **88**, 207403 (2002).
- ⁸R. Ruppin, J. Phys.: Condens. Matter **13**, 1811 (2001).
- ⁹H. Raether, *Surface Plasmons* (Springer, Berlin, 1988).
- ¹⁰R. Ziolkowski and E. Heyman, Phys. Rev. E **64**, 056625 (2001).
- ¹¹S. Cummer, Appl. Phys. Lett. **82**, 1503 (2003), preceding paper.